Cellular materials with tunable bistability integrating prominent soft and stiff properties

Abstract

Breaking the traditional boundary between the soft and stiff materials is being urgently desired for engineering materials that are overburdened by the demands of complicated and versatile tasks, but still remains a critical challenge. In this work, we pioneer bridging the soft-stiff responsive strategy of lightweight cellular materials through architecturally nesting two materials with contrasting properties. The proposed cellular materials can be reconfigured and switched between soft and stiff states, as demonstrated experimentally, theoretically and numerically. The soft state represents high perturbation sensitivity and prominent vibration isolation properties. The stiff state achieves strong load-carrying capability due to multi-synergistic mechanisms, with the crushing strength 1588 times as high as that in the soft state. The manipulable mechanical properties can be tuned across a broad design space while maintaining robust switchability. These advantages of the proposed bistate cellular materials offer promising application prospects from adaptive protection to shock absorption and beyond.

Keywords: Cellular materials; Mechanical properties; Soft-stiff switchability; Intelligent materials.

1. Introduction

Advances in the mechanical properties of architected materials are closely linked to the progress of engineering technology[1-3]. Through artificial design of their periodic cells, architected cellular materials achieve versatile mechanical characteristics at low densities, including tunable stiffness[4-6], ultra-high specific strength[7-9], damage-tolerant toughness[10-12] and superior fracture resistance[13-15]. Benefiting from advances in additive manufacturing[16-18], cellular material with extreme mechanical properties

can now be precisely fabricated and elaborately deployed in various application scenarios, such as bone regeneration[19-20], extreme environment robotics[21-22] and deep-space exploration[23-24]. However, as the tasks requiring these materials grow increasingly sophisticated and diverse, those offering only a single mechanical property advantage are increasingly inadequate to meet these complex demands.

To meet the requirements of intricate operating conditions, researchers are increasingly pursuing multifunctionality in architected cellular materials[25-27]. Designs incorporating multiple physical characteristics have emerged, such as combined sound absorption and deformation tolerance[28-29], or vibration isolation with energy absorption[30-31]. To streamline the design of such multifunctional materials, Li et al.[32] developed an interwoven dual-phase framework, which integrates noise-absorbing architected materials with isotropic elasticity by nesting diverse lattice units. Furthermore, cellular fabric materials with embedded self-locking lattice units realize adaptable load-bearing and protective capabilities through controlled cohesive pressure [33-34]. Remarkably, this fabric material composed of interlocking lattice cells exhibits non-Newtonian fluid behavior under small deformations while maintaining robust mechanical properties under large deformations [35]. This multistage, multi-plateau behavior, where mechanical properties evolve with loading progression, has inspired new approaches to reconciling traditionally incompatible properties in cellular materials[36-38]. Specifically, the mechanical response transits from a low-stiffness plateau (softer stage) to a high-stiffness plateau (stiffer stage) before failure, allowing for multiple targets protection leveraging the different plateau responses in different stages[39-41]. This multi-plateau transformation also optimizes the deformation process, resulting in significantly higher toughness compared to the single-plateau cellular materials[42-44]. The quasi-zero stiffness characteristics of the plateau stage possesses simultaneous vibration isolation and load-carrying capacity, making it a competitive candidate for applications like end-of-arm actuators and automotive load-carrying platforms[45]. However, this multi-plateau response depends critically on the loading

sequence. Designing cellular materials with sequence-independent multi-stage response still remains an unresolved challenge (**Figure 1Ai**).

To achieve independent state switching and retention, the bistable strategies[46-48] and shape memory polymers (SMPs)[49-50] offer explicit approaches. These methods utilize intricate geometries that transition from an original state to a new stable state under specific external stimuli, maintaining this new configuration upon stimulus removal[51-53]. Cellular materials with this behavior demonstrate wide geometric and mechanical tunability[54-55], making them highly suitable for applications such as gripping[56-58], shock mitigation[59-61], and logistic operations[62-64]. Furthermore, bimaterial configurations expand the design space for bistable cellular materials. For instance, dynamically reconfigurable granular metamaterials composed of discrete bimaterial architected particles have been developed [65]. Leveraging two or more materials with vastly different mechanical properties, bistable mechanical metamaterials that enable tailored multi-stage deformation responses have been created [66-70]. Bimaterial implementation further facilitates the optimization of material distribution, while these multi-stability characteristics provide the foundation for realizing manipulable stiff-soft switching cellular materials. To accomplish the lightweight design paradigm of stiff-soft switching for either uniaxial or spatial multi-axial, strategically balancing the advantages of soft and stiff material topological configurations is crucial. This optimization advances mechanical properties while maximizing material utilization, which also endows the cellular materials with manipulable mechanical properties across multiple orders of magnitude.

In this work, we develop bistate lightweight cellular materials to overcome current sequence limitations in the stiff-soft transition of architected cellular materials, bridging the gap between these responses. The manipulability of state switching of the proposed bistate lightweight cellular material is explored through comprehensive theoretical, experimental, and numerical investigations. This includes analyzing the mechanisms underlying the distinctive mechanical properties, e.g., compressive behavior, bending

behavior, and vibration isolation across different states. The distinct mechanical advantages offered in the manipulable soft and stiff states facilitate adaptive reconfiguration on demand, while unlocking the potential of cellular materials for in multi-target cushioning, tunable shock absorbers, and information storage.

2. Results and Analysis

2.1 Design strategy of bistate cellular materials

To achieve the stiff-soft manipulability with large region of cellular materials (**Figure 1Ai**), two base materials with contrasting properties are used to compose the stiff and soft components, respectively, that are architected in a nested manner within the structure as illustrated in **Figure 1Aii**. The geometry and wall-thickness of stiff and soft components require precise adjustment to simultaneously ensure switchability and lightweight performance. The stiff component constrains and supports the soft component, which transits between states through deformation (**Figure 1Aii**). The soft component consists of two similar cosine beams along with nesting beams, assembled with outer stiff components (**Figure S1**). One cosine beam is embedded within the stiff component to ensure reliable deformation behavior. Detailed design parameters are summarized in **Figure 3A and Table S1-S2**. When compressing the stiff component along the assembly direction, the soft component deforms and transforms into a new stable state (**Figure 1B**), which was experimentally verified using specimens fabricated by fused deposition modeling (FDM) and manufacturing details are provided in the Experimental Section. Whether stretched or compressed, the force direction is converted, allowing the current state to be maintained even after the external force is removed, achieving zero-energy state retention. In the initial state (soft state), the deformation occurs primarily through the soft component, which can carry a weight of only 20 g for a cellular material beam (**Figure 1Di**). After state transition shown in **Figure 1Di**i, the cellular material beam can carry 300 g at comparable deflection displacements, which is 15 times greater than in the soft state. In this stiff state, the

proposed cellular material can bear a human's weight while ensuring lightweight and compact dimensions due to the tight contact between stiff components (**Figure 1Diii**). Moreover, the bistate cellular materials can be constructed and integrated with various stiff materials including poly lactic acid (PLA), AlSi10Mg and stainless steel 316L (**Figure S2**), and the state transition can also be induced by thermal stimulus due to PLA's low glass transition temperature and its mechanical properties degrade under heat (**Figure S3**). Beyond material versatility, these units can be arranged in multi-axial configurations as displayed in **Figure 1D**, e.g., uniaxial, biaxial, and triaxial, enabling state-switching in multiple spatial directions with lightweight integration to unlock immense application potential of cellular materials (**Figure 1E**). The disturbance sensitivity in the soft state holds great promise for soft-cushioning and soft-landing applications. These materials cushion impacts for fragile objects like eggs and unmanned aerial vehicles (UAVs), and provide adaptive shock absorption. In stiff state, the high stiffness and strength facilitate load-bearing applications and hard impact protection. The demonstrated multifunctionality, adaptability, sustainability, and intelligence of these bistate cellular materials highlight the need for further exploration into tailoring their design parameters. Optimizing performance across both states is crucial for meeting diverse complex application requirements.

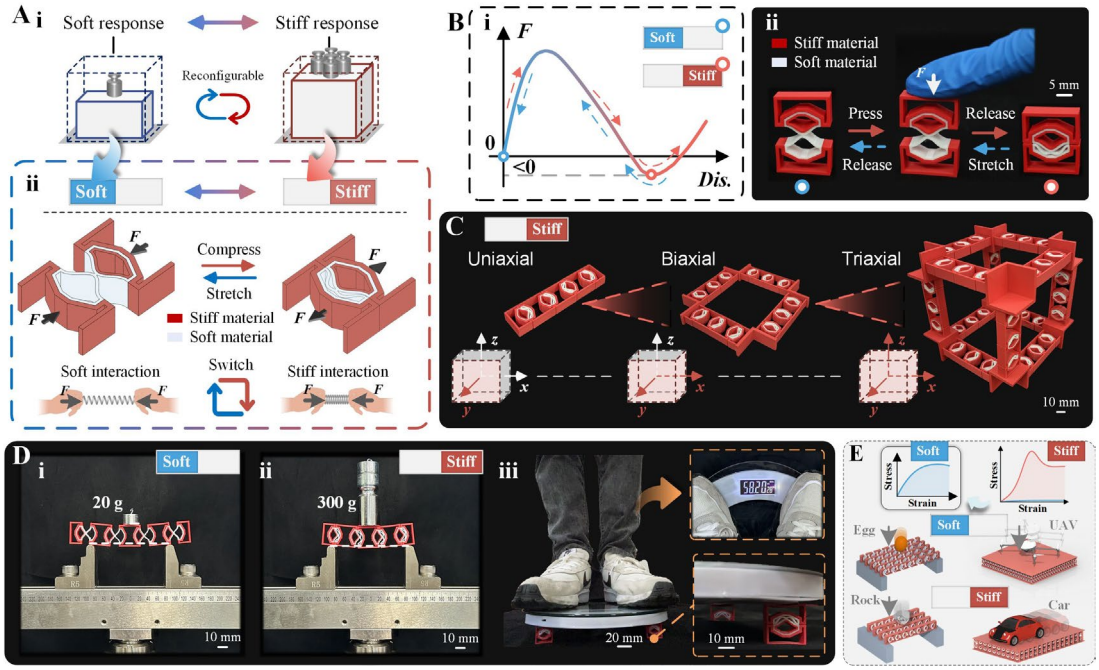

Figure 1. Design strategy for manipulable stiff-soft bistate cellular materials. (A) Concept of stiff-soft response manipulability: (i) switchable multi-response, (ii) schematic of bimaterial nesting strategy and corresponding soft and stiff states. (B) Switching path based on externally load-triggered, (ii) hot air-triggered and (iii) water-bath heating-triggered. (C) Evolution of multi-axial manipulable lattice materials from uniaxiality to tri-axiality. (D) Different mechanical performances in soft-stiff states. Flexural resistance in (i) soft state and (ii) stiff-state, as well as (iii) strong load-carrying capability in stiff-state. (E) Application prospects.

2.2 Bistable design of bistate cellular materials

Bistability is the key mechanism to realize the switchable mechanical performance of the proposed cellular materials. Therefore, we investigate this bistability mechanism through analytical modeling validated against numerical and experimental results in this section. **Figure 2Ai** illustrates the design parameters. The deformation of the cosine beam without embedded stiff components follows

$$\bar{w}(x) = \frac{h_1}{2}\left[1 - \cos\left(\frac{2\pi x}{l_2}\right)\right], \tag{1}$$

where h_1 and l_2 represent the cosine beam height and span. Under the lateral loading f acting on the top center of the cosine beam (**Figure 3Aii**), the non-rigid boundary constraints by the stiff component can be modeled as linear springs with stiffness K, which is dependent on the design parameters of stiff component as[71]:

$$K = \alpha\frac{I_1E_1}{h^{*3}} + \frac{3I_2E_2}{h^{*3}} \approx \alpha\frac{bE_1}{12Q_1^3}, \text{for } E_1 \gg E_2, Q_1 = \frac{h^*}{t_1}, \quad (2)$$

where, I_1 and I_2 are the moments of inertia of the stiff and soft restraining beams, respectively. E_1 and E_2 represent the Young's moduli of the stiff and soft materials, respectively (**Figure 2Aiv**). α is a coefficient, and h^* denotes the equivalent height of the cosine beam. The theoretical value of K calculated by Eq. (3) is further validated by comparison with the numerical results. According to the Eulerian-Bernoulli beam theory, the deflection $w(x)$ of a straight beam subjected to an axial force p is determined by the following equation[72]

$$E_2I_2\frac{d^4w(x)}{dx^4} + p\frac{d^2w(x)}{dx^2} = 0, \quad (3)$$

the normalized force-displacement response of cosine beam can be derived as (detailed in Section S3 from **Supporting Information**)

$$\begin{cases} F_1 = \left(\left(\left(\Delta - \frac{3}{2}\right)^2 - \frac{1}{4}\right)\frac{3\alpha E_1Q_2^2P}{\alpha E_1P + 2E_2Q_1^3} + 4\right)\frac{\pi^4\Delta}{2}, 0 \le \Delta \le \Delta_1, \Delta_3 \le \Delta \le 2 \\ F_3 = \frac{64}{3}\pi^2(4 - 3\Delta), \Delta_1 < \Delta < \Delta_3 \end{cases} \quad (4)$$

here

$$\Delta = \frac{d}{h^*}, F = \frac{l^{*3}f}{E_2I_2h^{*2}}, \quad (5)$$

where d is the deflection displacement, and l^* represents the equivalent span of the cosine beam. When $F_1(\Delta)$ and $F_3(\Delta)$ have only one intersection point, the normalized mechanical response of the curved beam is $F_1(\Delta)$. When they have three intersection points Δ_1, Δ_2 and Δ_3, the normalized force-displacement response follows Eq. (5). **Figure 2B** and **Figure S5** confirm strong agreement between theoretical, numerical, and experimental force-displacement curves and deformation modes. The details of numerical modeling are given in Experimental section.

Furthermore, the influences of design parameters on the bistable behavior are explored. For this sake, three main dimensionless parameters are investigated, i.e., wall-thickness ratio t_1/t_2, height-to-span ratio h_1/l_2, and press-in height ratio h_2/h_1. From the

normalized force-displacement curves in **Figure 2C**, it indicates that the constraint by the stiff component would become ineffective for too small wall-thickness t_1. Obviously, the stiffness K is mainly affected by the stiff component, which determines whether the bistability can be achieved. When K is less than a critical value K_{cr}, the proposed cellular material degenerates into a monostability (**Figure 2Aiii**). Besides the thin thickness of the stiff components, a narrow deformation space would also compromise the bistable behavior (**Figure 2D**). The retention force reinforces with the increase of t_1/t_2 and h_1/l_2, enhancing stability in stiff state. **Figure 2E** (from **Table S6**) presents the contours of the retention force in stiff state varying with t_1/t_2 and h_1/l_2 to depict the dependence of bistability on the design parameters. Note that the monostable retention force is assumed to be 0 in this figure. It indicates that the sensitivities of retention force to t_1/t_2 and h_1/l_2 are comparable, and the synergy of these configuration renders an enhanced influence on the retention force. Moreover, the positive force at normalized displacement Δ=2 indicates that the press-in height ratio h_2/h_1 must be less than 1 to ensure full contact in the switched stiff state (**Figure 2F**). However, a low l_2/h_1 causes monostable degeneration, as indicated in **Figure 2F**. This is because the space for transformation displacement is too narrow for the cosine beam to access the other stable state. In summary, the bistability of bistate cellular materials is highly dependent on the design configuration, the stiff state retention tunable by the wall-thickness ratio and height-to-span ratio, and the connectivity tailored by the press-in height ratio.

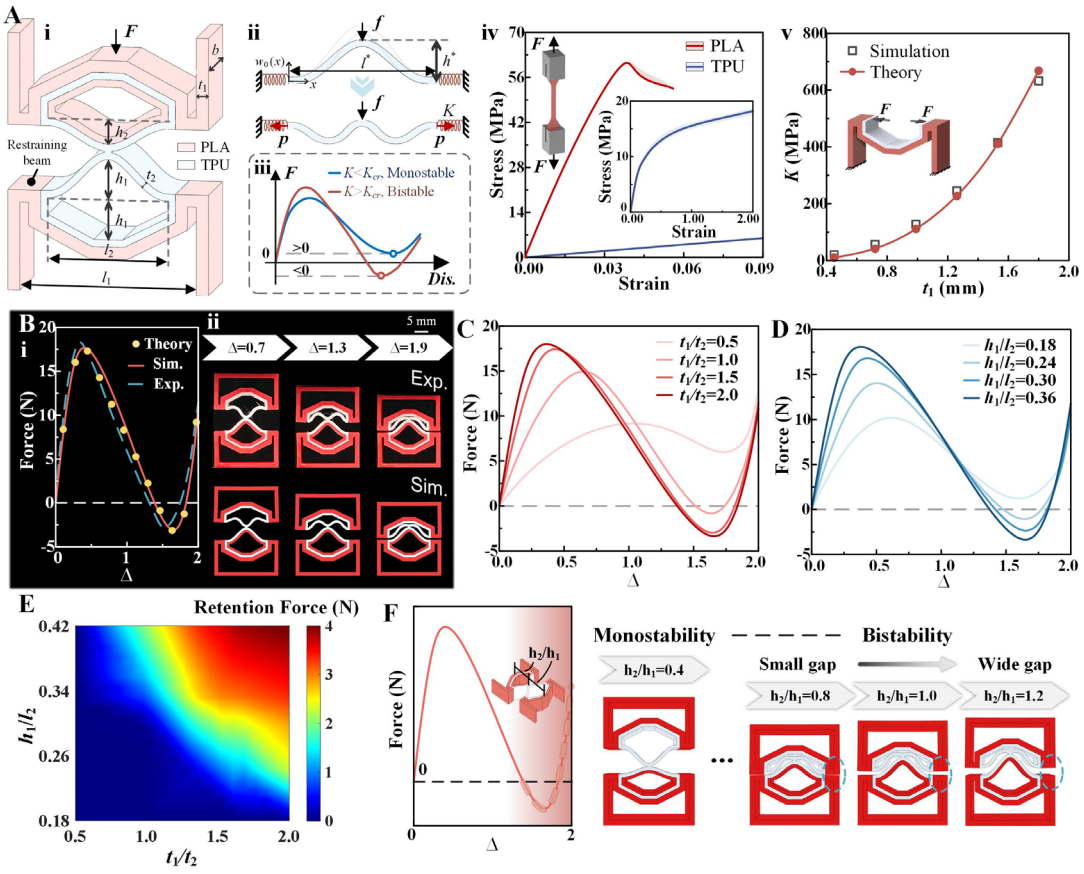

Figure 2. Bistability of the proposed cellular materials. (A) Analytical modeling: (i) schematic of design parameters; (ii) equivalent model with the stiff component equivalent to a linear spring of stiffness K; (iii) influence of the stiffness K on the bistable characteristic; (iv) material properties of TPU and PLA; (v) validation of the analytical model by comparison with the simulations in calculating K. (B) Comparison between analytical, numerical and experimental results: (i) normalized force-displacement curves and (ii) deformation modes. (C) Normalized force-displacement curves at different t_1/t_2. (D) Normalized force-displacement curves at different h_1/l_2. (E) Combined influence of t_1/t_2 and h_1/l_2 on retention force in stiff state (the monostable retention force is 0). (F) Influences of t_1/t_2 and h_2/h_1 on the bistability.

2.3 Switchability of mechanical performances

To demonstrate the switchability of mechanical performances, we first conducted compressive tests on the bistate cellular materials, as illustrated in **Figure 3A** (detailed in Experimental Section and **Figure S4**). Due to the disparity in load transfer paths in different states, deformation localizes primarily within the soft component in the soft state and the stiff component in the stiff state (**Figure 3Ai**). Consequently, the compressive stress in the stiff state is significantly higher than in the soft state (**Figure 3Aii**). The crushing strength (defined as the maximum crushing stress and representing

the load-bearing capability) of the bistate cellular material in the stiff state is strengthened by 1588 and 50.69 times compared to the soft state, when using stainless steel 316L and PLA as the stiff materials, respectively. This three-order-of-magnitude difference of strengths in stiff and soft states demonstrates the strong adaptability of the soft-stiff-bistate manipulable cellular materials, and this dramatic strength difference and excellent lightweight are highly competitive compared to existing work (**Figure 3Aiii**) [65, 70, 73-76].

The mechanical advantage of the proposed cellular material can be further extended to other loading conditions such as bending, as shown in **Fig. 3B** [34, 73]. We further fabricated the specimen of bistate cellular materials with the uniaxial arrangement and carried out the three-point bending tests with a span of 90 mm (**Figure 3Bi**). The flexural resistance (maximum bending load) of the bistate cellular materials in the stiff state can be up to 15.36 times greater than in the soft state. Under the soft state, the connection nodes/joints of the soft components bear most of the loads, making it yield to large deformation under the minor perturbations or loads. Upon switching to the stiff state, robust interactions develop between the stiff components. Consequently, the flexural resistance in this state largely depends on the configuration of the stiff components and the stability of the stiff state, leading to a sharp rise of the flexural resistance relative to the soft state.

In addition, the lower stiffness and strength in the soft state endow the material with exceptional vibration isolation properties. To demonstrate this, we constructed a vibration isolation platform utilizing bistate cellular material as its core component. The transmission indicator T is defined as the logarithmic ratio of output amplitude A_{out} to input amplitude A_{in}:

$$T = 20\lg(A_{\text{out}}/A_{\text{in}}). \quad (6)$$

A negative transmission corresponds to effective vibration isolation, indicating that the input vibration energy is transferred. In the soft state, the free and flexible soft components act can be as soft connecting springs, which together with the stiff

components (function as mass blocks) form an ideal localized resonance damper that effectively transferers the vibration energy (**Figure 3Ci-ii**). Conversely, in the stiff state, the soft components are constrained, and loads are transmitted directly through the stiff components, hindering the mechanism of vibration energy transition. As shown in the frequency-transmission spectra (**Figure 3Ciii**), the bistate cellular material in the soft state exhibits a broad frequency range of vibration isolation and a low minimum transmission. In contrast, transmission in stiff state remains consistently greater than zero. In summary, this nesting strategy successfully integrates two contrasting mechanical properties, enabling controlled state manipulation and retention, achieving performance differences spanning up to three orders of magnitude. This capability fundamentally challenges the conventional paradigm where the mechanical behavior of materials is determined after fabrication.

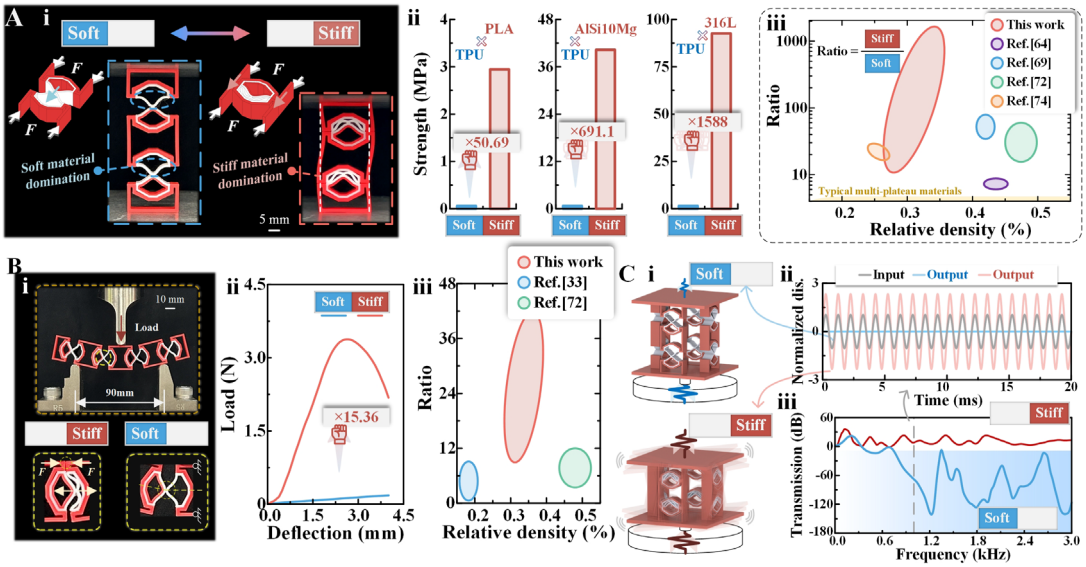

Figure 3. Mechanical characteristics of the bistate cellular materials in soft and stiff states. (A) Compression behavior: (i) deformation mechanisms, (ii) comparison of strengths using different stiff-materials, and (iii) comparison of this work with existing work. (B) Flexural behavior: (i) schematic and deformation of three-point bending test, (ii) force-deflection curves, and (iii) comparison of this work with existing work. (C) Vibration isolation properties: (i) schematic of state-dependent mechanisms, (ii) normalized displacement-time curves at 1000 Hz, (iii) transmission-frequency spectra.

2.4 Mechanical behaviors in soft state

In this section we focus on the behaviors and underlying mechanisms of the soft state (the initial state after fabrication), especially on how design parameters influence the mechanical properties. Besides the wall-thickness ratio and the height-to-span ratio, the shape of stiff component emerges as a critical parameter, meaningfully altering the connection geometry and load transfer direction (**Figure 4Ai**). As illustrated in **Figure 4Aii** and **Table S7**, the crushing strengths of parallelogram-shaped and rectangle-shaped stiff component are promoted by 41.18% and 13.72% relative to the trapezoidal shaped case, respectively. The parallelogram and trapezoidal shapes both direct the load along the direction towards the soft component at an angle to the applied loading direction. However, the parallelogram shape generates additional friction, and requires greater crushing stress to overcome this friction, enhancing its load-carrying capacity. Conversely, friction in the trapezoidal shape opposes the loading direction, partially counteracting crushing strength. Additionally, the crushing stress also rises with increasing wall-thickness ratio and height-to-span ratio as evidenced in **Figure 4E**. The press-in height ratio primarily affects the connectivity in the stiff state, and has little influence on the soft-state mechanical properties. On the other hand, variations in design configuration, however, show minimal effect on flexural properties. Most loads and deformations concentrate at the connective nodes of the soft components, resulting in low bending strength and consequently significant flexibility (**Figure 4B**). This pronounced flexibility makes it particularly effective for resisting soft impacts and protecting delicate objects, such as eggs, UAVs (**Figure 2Biv**), while also offering benefits for system vibration isolation.

Based on the vibration modes obtained from the verified numerical simulations (**Figure 4C and Figure S6**), the output displacement is effectively isolated at low frequencies (white region in **Figure 4Ci**). As plotted in **Figure 4Cii**, the bandgap from bandgap structures is consistent with the vibration isolation transmission region is defined as low as below -20 dB, which further ensure that the output displacement

response is fully attenuated. In general, the bistate cellular materials in its soft state still exhibits a low onset frequency for vibration isolation and a wide bandwidth. The synergy between soft and stiff components results in an effective spring-oscillator system. Furthermore, the advantages in onset frequency and bandwidth are improved when using AlSi10Mg or stainless steel 316L as stiff material (**Figure 4Di**), attributable to the reinforced oscillator mass. Compared to PLA as the stiff material, the 316L stainless steel improves the onset vibration isolation frequency by 97.82% and reduces the minimum transmission by 29.63%. The observed differences in bandgap characteristics arise primarily from the variation in material stiffness and density, which affects the wave speed and modal count. Softer stiff materials like PLA support multiple local resonances, leading to multiple fragmented band gaps, while stiffer materials such as AlSi10Mg and 316L suppress higher-order modes, resulting in broader and more continuous bandgaps. In addition, applying a small pre-strain compresses the soft components (can also be regarded as applying a certain load), reducing the stiffness and yielding superior vibration isolation performance (**Figure 4Dii**). The onset isolation frequency with 5.0% pre-strain occurs 99.45% earlier than without pre-strain, demonstrating that bistate cellular materials appears advanced vibration isolation characteristics while maintaining exceptional load-carrying capacity. As shown by the design parameters in **Figure 4E**, the onset vibration isolation frequency delays progressively with increasing the wall-thickness ratio t_1/t_2. This occurs because the stiffness of the soft component (acting as the spring in the localized resonance damper) increases with t_1. The height-to-span ratio similarly affects onset frequency and minimum transmission, although the effect is less pronounced.

In conclusion, bistate cellular materials are flexible and tailorable in both crushing strength and vibration isolation. These properties can be controlled independently through different configurations, promoting the multifunctionality of the material in its soft state.

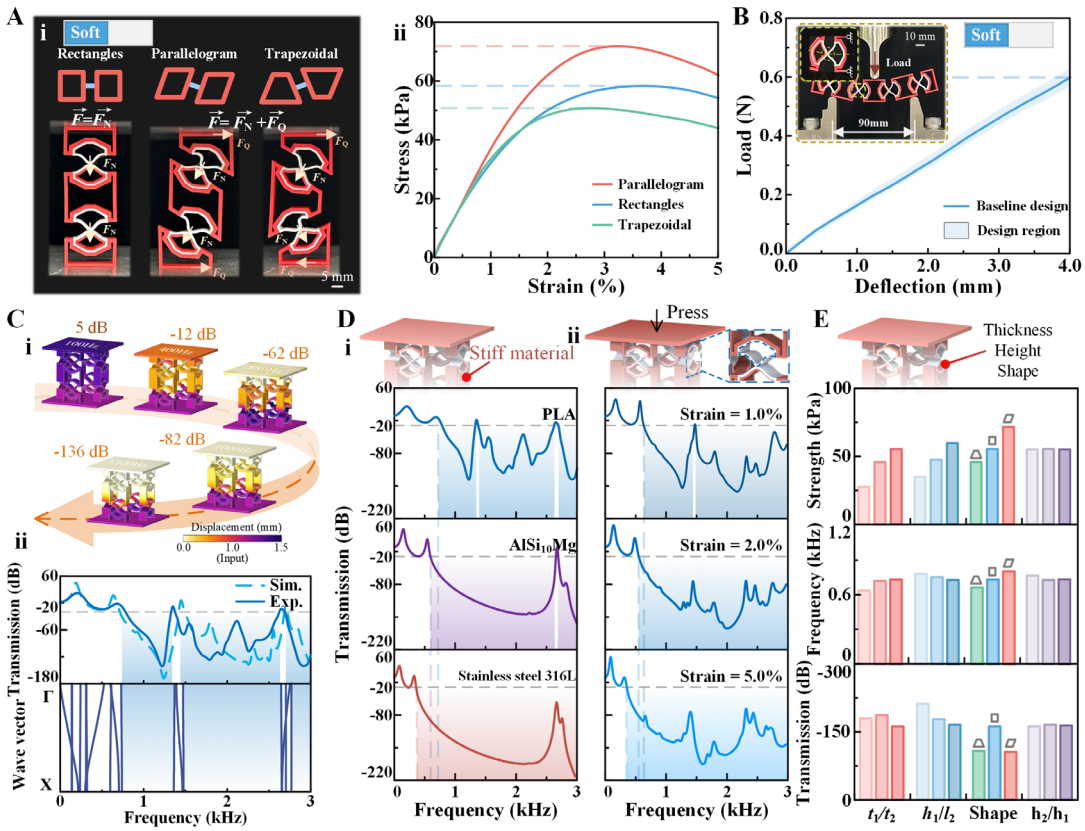

Figure 4. Mechanical behaviors of the bistate cellular materials in soft state. (A) Compression behavior under different shaped configuration: (i) Deformation modes and (ii) stress-strain curves. (B) Deflection behavior through three-point bending tests. (C) Vibration isolation behavior: (i) Vibration modes, and (ii) comparison of transmission and band structure results between simulations and experiments. (D) Transmission-frequency spectra with various (i) stiff materials and (ii) pressed strain. (E) Strength and vibration isolation properties for different design parameters.

2.5 Mechanical behaviors in stiff state

When switched to the stiff state, the crushing process of the material can be divided into three stages, i.e., a slow climb stage, a rapid surge stage and a decline stage, as shown in **Figure 5A**. Initially, due to incomplete contact of the stiff component and manufacturing tolerances, the compressive stress arises slow from further interaction between the soft and the stiff components. Subsequently, the crushing stress grows sharply as deformation localizes within the stiff components (**Figure 5B**). The crushing stress reaches the maximum until the buckling of stiff components occurs, after which the stress decreases. Since deformation and buckling are mainly governed by the stiff components, the crushing strength is highly dependent on their wall thickness. As

shown in **Figure 5Bi**, the region of high von-Mises stress expands as the wall-thickness ratio t_1/t_2 increases. Correspondingly, the crushing strength is also upgraded with the increase of t_1/t_2 (**Figure 5Ai, Av**). The modeling methodology for von-Mises stresses is described and validated in Experiments Section. Notably, the crushing strength for t_1/t_2=1.6 is 6.83 times greater than that for t_1/t_2=1.0 (**Figure 5Aiv**, **Av, Table S7**), despite similar corresponding strains. Furthermore, increasing the height-to-span ratio h_1/l_2 prolongs the strain required to reach the maximum stress without compromising the crushing strength (**Figure 5Aii** and **Bii**). A slight strength reduction (9.86% within acceptable tolerance) occurs due to partial buckling of stiff components before full contact (**Figure 5Aiv**, **Table S7**). Overall, judicious selection of the wall-thickness ratio and the height-to-span ratio effectively tunes the compressive behavior of bistate cellular materials (**Figure 5Aiii**). However, varying the inclined shape (parallelogram, trapezoid) does not advance the load-carrying performances (**Figure 5Aiii, Biii**). Rectangular stiff components exhibit much higher crushing strength, 2.51 times and 1.92 times greater than the parallelogram and trapezoid shapes, respectively (**Figure 5Aiv**, **Av, Table S7**). This performance difference stems from the inclined load transfer direction in parallelogram and trapezoid shapes, which induces slippage along the inclined surfaces, and substantially reduces the load-carrying capacity.

Contrary to the crushing response observed (**Figure 5C**, **Table S8**), flexural properties in bistate cellular materials can be strengthened and tailored not only by wall thickness but also through adjusting the ratios h_1/l_2, h_2/h_1, as well as shape selection. With the reinforcement of retention force, three-point bending experiments revealed that the deformation primarily localizes within the soft component, rendering a deformation mode where the curved beam rotates around a pivot point on the stiff component until it transits to the soft state and fails. Consistent with the influence of design parameters on retention force, higher t_1/t_2 and h_1/l_2 correlate with larger flexural strength (**Figure 5Ciii**). Increasing these ratios also lead to the decrease and increase of the deflections, respectively. While the expand of the press-in height ratio h_2/h_1 does

not affect the retention force, a larger h_2/h_1 causes the rotation center to shift along the curved beam during bending (**Figure 5Ci, Di**). This implies a decreasing force arm, which enlarge the resistance force. Consequently, the peak load rises with h_2/h_1, and the corresponding deflection also raise, which is the most significant effect among the proposed configurations (**Figure 5Ciii**, **Table S8**). Quantitatively, the peak load at h_2/h_1= 1.2 is 2.65 times greater than at h_2/h_1= 0.8. Bending behavior is also sensitive to the shape of the stiff component. The contact surfaces inclined against the loading direction provide greater load resistance during the deformation of the soft component, thereby increasing flexural strength (**Figure 5Cii**, **Dii**). Compared with the rectangular shapes, the parallelogram configuration exhibits a 23.96% higher peak load (**Figure 5Ciii**, **Table S8**). Due to the multi-synergistic mechanisms between the stiff and soft components, the proposed bistate cellular materials exhibit superior crushing and bending performance in the stiff state. These properties can be precisely tuned through the configuration design.

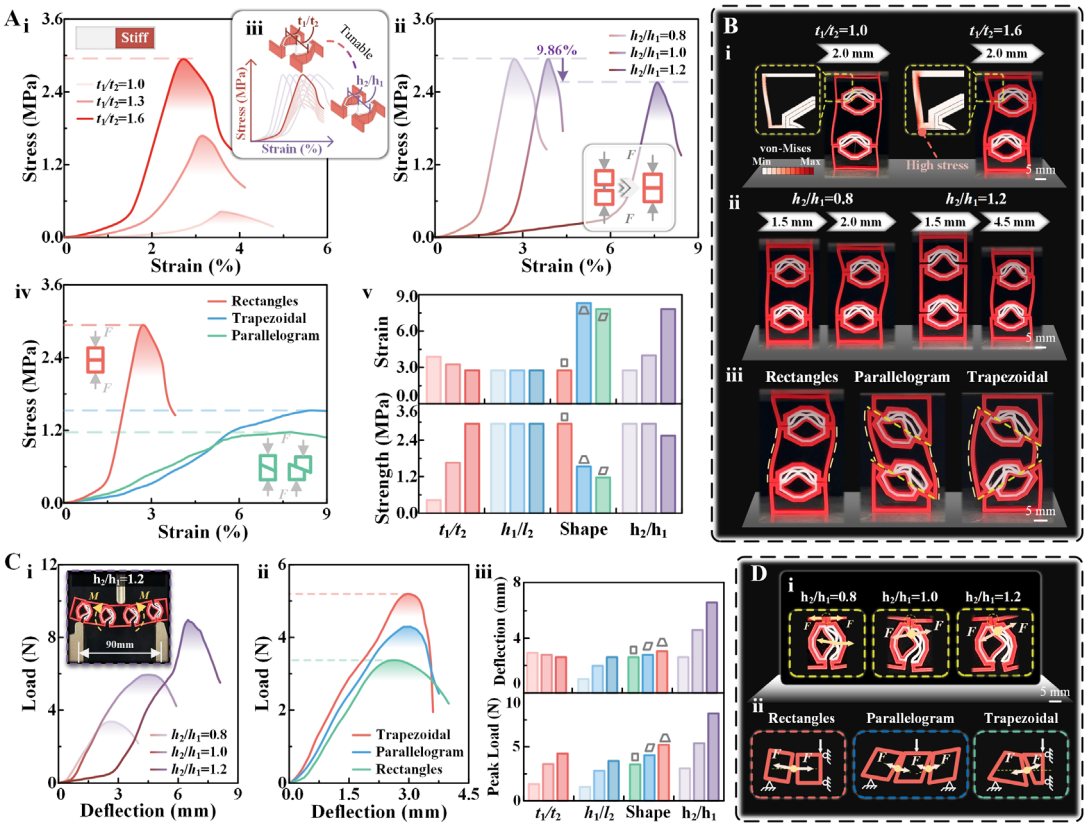

Figure 5. Mechanical behaviors of the bistate cellular materials in stiff state. (A) Compression

stress-strain curves (i) under different t_1/t_2, (ii) under different h_2/h_1, (iii) showing tunability, (iv) under different shapes, and (v) comparing their strengths and corresponding strains. (B) Compression deformation modes under different (i) t_1/t_2, (ii) h_2/h_1 and (iii) shapes. (C) Three-point bending behaviors: stress-strain curves under different (i) h_2/h_1 and (ii) shapes, and (iii) comparison of peak loads and corresponding deflections. (D) Three-point bending deformation modes under different (i) h_2/h_1 and (ii) shapes.

3. Conclusions

This work proposes a design paradigm of bistate cellular materials, filling a gap in achieving manipulable stiff-soft performance across a large order-of-magnitudes with different stable state. Through integrated theoretical analysis, experimental validation, and numerical simulation, it is demonstrated that the proposed cellular materials can be purposely switched between distinct states by implementing a bimaterial nesting design strategy, scalable from uniaxial to triaxial configurations. These bistate cellular materials also enables tailoring of the mechanical properties in each state, including stiffness of base material, wall-thickness ratio t_1/t_2, height-to-span ratio h_1/l_2, press-in height ratio h_2/h_1 and the geometry of the stiff component.

In soft state, deformation and strength are governed by the hinge points of cosine beams within the soft component, making them highly sensitive to minor perturbations. These characteristics allow advanced applications in flexible cushioning and vibration isolation, offering simultaneous load-bearing capability and superior vibration isolation performance at specific compressive strains. After switching to the stiff state, multi-synergetic mechanisms emerge. Interactions between stiff components and state retention forces generated by the soft components collectively improve the crushing and bending resistance. Compared with the soft state, the crushing strength and peak bending load of the stiff state are strengthened by 1588 times and 40.72 times, respectively. In the pursuit of ultra-lightweight properties, this stiff-soft switching performances with dramatic mechanical difference can be featured as a significant advancement over existing work. The crushing stress and corresponding strain can be further promoted with programmability demonstrated through t_1/t_2 and h_2/h_1 under compression. In contrast, the flexural strength is most significantly strengthened by

press-in height ratio h_2/h_1, due to the shift in the rotational pivot point during deformation.

The inherent reconfigurability and versatility of stiff-soft manipulable cellular materials paves a new pathway for advancing intelligent, sustainable material systems. These materials hold significant promise for pioneering multi-state switching and multi-scale designs that incorporate exceptional strength-to-weight ratios, allowing for diverse applications in sophisticated and extreme environments, such as wearable devices, deep-sea robotics, and aerospace applications.

4. Experimental Section

Manufacturing and experiment process: The bistate cellular materials with different unit cells were fabricated by a FDM printer Bambu Lab X1 Carbon from Shenzhen Tuozhu Technology Co. Ltd. using the PLA and TPU filaments, as well as a SLM printer WXL-340 from Xiamen Wuxinglong Technology Co. Ltd. using AlSi10Mg and 316L stainless steel powders. The configuration parameters are summarized in **Table S2**, while the manufacturing process parameters are summarized in **Table S3 and Table S4**. Employing the universal testing machines LD23.103 and LD26.504 from Lishi (Shanghai) Instruments Co. Ltd., quasi-static compressive and three-point bending tests were conducted to explore the mechanical performances. The specimens were located on the supporter, with compression applied via an indenter or clamp moving downwards at a velocity of 1 mm/min. Deformation processes were recorded using a digital camera. The vibration isolation performance was assessed by inputting a 1 mm amplitude signal through the shaker. The resulting detector output signal was amplified and recorded for computer analysis. Detailed experimental setups are illustrated in **Figure S4**.

Numerical simulation: The commercial finite element software ABAQUS/Standard (version 2020) was employed to verify bistable behavior and investigate the compression response of the bistate cellular materials. In the model, the bottom surface was constrained, with compressive displacement applied axially to the

top surface. The contact surfaces between the soft component and the stiff component were subject to tie constraint. The surface-to-surface contact algorithms were implemented only for the contact between stiff and soft components, as well as between two adjacent stiff components after sufficient deformation, where the friction coefficient was set as 0.25.

The transmission-frequency response and wave propagation behavior were simulated using COMSOL Multiphysics 6.2 with the solid mechanics module. The output displacement was detected under a 1 mm input amplitude, and the transmission was calculated according to Eq. (1) to obtain transmission-frequency response. The wave propagation characteristics follow the equations below

$$(\boldsymbol{K} - \omega^2 \boldsymbol{M})\boldsymbol{U} = 0, \boldsymbol{U}(\boldsymbol{R} + \boldsymbol{A}) = e^{ikA}\boldsymbol{U}(\boldsymbol{R}), \quad (7)$$

where $\boldsymbol{K}$ and $\boldsymbol{M}$ denote the stiffness matrix and the mass matrix, respectively. ω and $\boldsymbol{U}$ represent the natural frequency and node displacement vector, respectively. The relationship between the position vector of a boundary point $\boldsymbol{R}$, the lattice cell vector $\boldsymbol{A}$, and the wave vector k was also depicted. The wavevector direction was scanned across the first irreducible Brillouin zone, and the Bloch-Floquet boundary conditions were adopted to further analyze the band structures.

The material properties followed the experimental data shown in **Figure 3Aiv**. The numerical simulation results and comparisons with experimental data are presented in **Figure S5-S7**, showing discrepancies within acceptable range.

Supporting Information

The supporting information are available from the author or the Wiley Online Library.

Acknowledgments

F. Yang acknowledges the financial support from National Natural Science Foundation of China (12472077), the Fundamental Research Funds for the Central

Universities (22120240353), State Key Laboratory of Structural Analysis, Optimization and CAE Software for Industrial Equipment (GZ23107), and Shanghai Gaofeng Project for University Academic Program Development.

Conflict of interests

The authors declare that there is no interest of any nature or kind involved in the process of the creation of our article.

References

[1] X. Zheng, H. Lee, T. H. Weisgraber, M. Shusteff, J. DeOtte, E. B. Duoss, J. D. Kuntz, M. M. Biener, Q. Ge, J. A. Jackson, S. O. Kucheyev, N. X. Fang, C. M. Spadaccini, *Science* **2014**, 344, 1373.

[2] M. Kadic, G. W. Milton, M. van Hecke, M. Wegener, *Nature Reviews Physics* **2019**, 1, 198.

[3] X. Zhang, F. Zangeneh-Nejad, Z.-G. Chen, M.-H. Lu, J. Christensen, *Nature* **2023**, 618, 687.

[4] M. I. N. Rosa, K. Karapiperis, K. Radi, E. Pescialli, D. M. Kochmann, *Advanced Materials* **2025**.

[5] X. Fang, D. Yu, J. Wen, Y. Dai, M. R. Begley, H. Gao, P. Gumbsch, *Nature* **2025**, 639, 639.

[6] Y. Liu, Y. Wang, H. Ren, Z. Meng, X. Chen, Z. Li, L. Wang, W. Chen, Y. Wang, J. Du, *Nature Communications* **2024**, 15.

[7] P. Serles, J. Yeo, M. Haché, P. G. Demingos, J. Kong, P. Kiefer, S. Dhulipala, B. Kumral, K. Jia, S. Yang, T. Feng, C. Jia, P. M. Ajayan, C. M. Portela, M. Wegener, J. Howe, C. V. Singh, Y. Zou, S. Ryu, T. Filleter, *Advanced Materials* **2025**, 37.

[8] J. Ding, Q. Ma, X. Li, L. Zhang, H. Yang, S. Qu, M. Y. Wang, W. Zhai, H. Gao, X. Song, *Advanced Science* **2024**, 11.

[9] Y. J. Wang, X. Zhang, Z. H. Li, H. J. Gao, X. Y. Li, *P Natl Acad Sci USA* **2022**, 119.

[10] P. Wang, F. Yang, B. Zheng, P. Li, R. Wang, Y. Li, H. Fan, X. Li, *Advanced Functional Materials* **2023**, 33.

[11] H. Xing, X. He, Y. Wang, X. Zhang, L. Li, Y. Wang, Z. Cheng, H. Wu, Q. Ge, X. Li, *Materials Today* **2023**, 68, 84.

[12] P. Zhang, X. Chen, P. Yu, K. Zhao, H. Ma, S. Liu, H. Tan, V. Laude, M. Kadic, *Journal of the Mechanics and Physics of Solids* **2025**, 197.

[13] Y. Wang, K. Wu, X. Zhang, X. Li, Y. Wang, H. Gao, *Science Advances* **2024**, 10.

[14] Z. Wang, K. Wu, J. Ding, J. Jin, Y. Zhou, M. Li, Y. Yao, L. He, Z. Song, Y. Ni, *Advanced Materials* **2025**.

[15] Z. Gao, X. Zhang, Y. Wu, M.-S. Pham, Y. Lu, C. Xia, H. Wang, H. Wang, *Nature Communications* **2024**, 15.

[16] J. Wu, Y. Zhang, F. Yang, F. Jiang, X. Xu, Y. Tan, L. Su, *Additive Manufacturing* **2023**, 76.

[17] J. U. Surjadi, C. M. Portela, *Nature Materials* **2025**, 24, 493.

[18] X. Chen, J. Moughames, Q. Ji, J. A. I. Martínez, H. Tan, G. Ulliac, V. Laude, M. Kadic,

Journal of the Mechanics and Physics of Solids **2022**, 169.

[19] H. M. A. Kolken, S. Janbaz, S. M. A. Leeflang, K. Lietaert, H. H. Weinans, A. A. Zadpoor, *Materials Horizons* **2018**, 5, 28.

[20] J. Gao, X. Cao, M. Xiao, Z. Yang, X. Zhou, Y. Li, L. Gao, W. Yan, T. Rabczuk, Y.-W. Mai, *Materials Science and Engineering: R: Reports* **2023**, 156.

[21] G. Li, X. Chen, F. Zhou, Y. Liang, Y. Xiao, X. Cao, Z. Zhang, M. Zhang, B. Wu, S. Yin, Y. Xu, H. Fan, Z. Chen, W. Song, W. Yang, B. Pan, J. Hou, W. Zou, S. He, X. Yang, G. Mao, Z. Jia, H. Zhou, T. Li, S. Qu, Z. Xu, Z. Huang, Y. Luo, T. Xie, J. Gu, S. Zhu, W. Yang, *Nature* **2021**, 591, 66.

[22] G. Li, T.-W. Wong, B. Shih, C. Guo, L. Wang, J. Liu, T. Wang, X. Liu, J. Yan, B. Wu, F. Yu, Y. Chen, Y. Liang, Y. Xue, C. Wang, S. He, L. Wen, M. T. Tolley, A. M. Zhang, C. Laschi, T. Li, *Nature Communications* **2023**, 14.

[23] Y. Lai, C. Zang, G. Luo, S. Xu, R. Bo, J. Zhao, Y. Yang, T. Jin, Y. Lan, Y. Wang, L. Wen, W. Pang, Y. Zhang, *Science Advances* **2024**, 10.

[24] W. Wu, R. Xia, G. Qian, Z. Liu, N. Razavi, F. Berto, H. Gao, *Progress in Materials Science* **2023**, 131.

[25] H. Yang, W.-J. Wang, O. Wyman, W. Zhai, L. Ma, D. Pasini, *Materials Today* **2025**.

[26] C. Yue, W. Zhao, F. Li, B. Li, L. Liu, Y. Liu, J. Leng, *Advanced Functional Materials* **2024**, 34.

[27] K. Liu, R. Sun, C. Daraio, *Science* **2022**, 377, 975.

[28] X. Li, J. W. Chua, X. Yu, Z. Li, M. Zhao, Z. Wang, W. Zhai, *Advanced Science* **2023**, 11.

[29] J. Zhang, J. Liu, A. Souslov, M. T. P. Prado, J. Segurado, M. Haranczyk, J. Christensen, *Advanced Materials* **2025**, 37.

[30] L. Li, J. Wu, F. Yang, P. Li, G. Lu, H. Fan, J. Zhao, N. Zhang, Q. Yang, *Composites Part B: Engineering* **2025**, 291.

[31] L. Li, F. Yang, Z. Guo, J. Wu, G. Lu, H. Fan, *Virtual and Physical Prototyping* **2024**, 19.

[32] Z. Li, K. Zeng, Z. Guo, Z. Wang, X. Yu, X. Li, L. Cheng, *Advanced Functional Materials* **2024**.

[33] Y. Tian, K. Chen, H. Zheng, D. R. Kripalani, Z. Zeng, A. Jarlöv, J. Chen, L. Bai, A. Ong, H. Du, G. Kang, Q. Fang, L. Zhao, H. J. Qi, Y. Wang, K. Zhou, *Advanced Science* **2023**, 10.

[34] Y. Wang, L. Li, D. Hofmann, J. E. Andrade, C. Daraio, *Nature* **2021**, 596, 238.

[35] W. Zhou, S. Nadarajah, L. Li, A. G. Izard, H. Yan, A. K. Prachet, P. Patel, X. Xia, C. Daraio, *Science* **2025**, 387, 269.

[36] C. Coulais, A. Sabbadini, F. Vink, M. van Hecke, *Nature* **2018**, 561, 512.

[37] Z. Meng, M. Liu, Y. Zhang, C. Q. Chen, *Journal of the Mechanics and Physics of Solids* **2020**, 144.

[38] Q. Zhang, D. Guo, G. Hu, *Advanced Functional Materials* **2021**, 31.

[39] C. Liu, M. S. Pham, *Advanced Materials* **2023**, 36.

[40] Q. Zeng, S. Duan, Z. Zhao, P. Wang, H. Lei, *Advanced Science* **2022**, 10.

[41] Y. Tian, X. Zhang, B. Hou, A. Jarlöv, C. Du, K. Zhou, *Proceedings of the National Academy of Sciences* **2024**, 121.

[42] J. U. Surjadi, B. F. G. Aymon, M. Carton, C. M. Portela, *Nature Materials* **2025**.

[43] J. Wu, F. Yang, L. Li, P. Li, X. Xu, Y. Zhang, *International Journal of Mechanical Sciences*

2024, 283.

[44] S. Yin, W. Guo, H. Wang, Y. Huang, R. Yang, Z. Hu, D. Chen, J. Xu, R. O. Ritchie, *Journal of the Mechanics and Physics of Solids* **2021**, 149.

[45] C. Zeng, L. Liu, Y. Hu, W. Zhao, X. Xin, Y. Liu, J. Leng, *Advanced Functional Materials* **2024**, 34.

[46] B. Haghpanah, L. Salari‐Sharif, P. Pourrajab, J. Hopkins, L. Valdevit, *Advanced Materials* **2016**, 28, 7915.

[47] R. Xu, Y. He, C. Chen, J. Sun, X. Li, M. H. Lu, Y. F. Chen, *Advanced Science* **2025**.

[48] Y. Liu, Z. Meng, Y. Wang, C. Q. Chen, *Journal of the Mechanics and Physics of Solids* **2025**, 196.

[49] T. Xie, *Nature* **2010**, 464, 267.

[50] C. Ni, D. Chen, Y. Yin, X. Wen, X. Chen, C. Yang, G. Chen, Z. Sun, J. Wen, Y. Jiao, C. Wang, N. Wang, X. Kong, S. Deng, Y. Shen, R. Xiao, X. Jin, J. Li, X. Kong, Q. Zhao, T. Xie, *Nature* **2023**, 622, 748.

[51] Y. Liu, F. Pan, F. Xiong, Y. Wei, Y. Ruan, B. Ding, K. Yang, Y. Chen, *Advanced Functional Materials* **2023**, 33.

[52] R. Xu, C. Chen, J. Sun, Y. He, X. Li, M.-H. Lu, Y. Chen, *International Journal of Extreme Manufacturing* **2023**, 5.

[53] L. Ai, S. Yin, W. He, P. Zhang, Y. Li, *Nature Communications* **2024**, 15.

[54] L. Wu, D. Pasini, *Nature Communications* **2024**, 15.

[55] L. Wu, D. Pasini, *Advanced Materials* **2023**, 35.

[56] S. Rahman, L. Wu, A. El Elmi, D. Pasini, *Advanced Functional Materials* **2023**, 33.

[57] B. Shahryari, H. Mofatteh, A. Sargazi, A. Mirabolghasemi, D. Meger, A. Akbarzadeh, *Advanced Functional Materials* **2024**, 35.

[58] P. Ducarme, B. Weber, M. van Hecke, J. T. B. Overvelde, *Proceedings of the National Academy of Sciences* **2025**, 122.

[59] H. Yang, J. Zhang, J. Wang, J. Hu, Z. Wu, F. Pan, J. Wu, *Advanced Functional Materials* **2024**, 35.

[60] X. Xin, C. Lin, B. Li, R. Zhang, C. Zeng, L. Liu, Y. Liu, J. Leng, *International Journal of Extreme Manufacturing* **2024**, 7.

[61] F. Pan, Y. Li, Z. Li, J. Yang, B. Liu, Y. Chen, *Advanced Materials* **2019**, 31.

[62] R. Ma, L. Wu, D. Pasini, *Advanced Functional Materials* **2023**, 33.

[63] Z. Liu, H. Fang, J. Xu, K. W. Wang, *Advanced Science* **2023**, 10.

[64] L. Wu, Y. Lu, P. Li, Y. Wang, J. Xue, X. Tian, S. Ge, X. Li, Z. Zhai, J. Lu, X. Lu, D. Li, H. Jiang, *Advanced Science* **2023**, 11.

[65] Z. Meng, H. Yan, Y. Wang, *Science Advances* **2024**, 10.

[66] Z. Meng, M. Liu, H. Yan, G. M. Genin, C. Q. Chen, *Science Advances* **2022**, 8.

[67] H. Yang, W. J. Wang, J. Z. Zhu, L. Ma, D. Pasini, W. Zhai, *Advanced Functional Materials* **2025**, 35.

[68] X. Wang, Z. Li, J. Deng, T. Gao, K. Zeng, X. Guo, X. Li, W. Zhai, Z. Wang, *Advanced Functional Materials* **2024**, 35.

[69] J. He, Y. Wang, H. Tang, G. Zhang, K. Dong, D. Wang, L. Xia, Y. Xiong, *Materials Horizons*

2025.

[70] Y. Wei, F. Pan, X. Lin, L. Zhang, J. Xiang, Y. Chen, *Advanced Materials* **2024**, 37.

[71] J. Hua, Y. Zhou, C. Q. Chen, *International Journal of Mechanical Sciences* **2024**, 272.

[72] J. Qiu, J. H. Lang, A. H. Slocum, *Journal of Microelectromechanical Systems* **2004**, 13, 137.

[73] J. Yi, R. Lyu, Y. Li, C. Wan, K. Zhang, *Advanced Functional Materials* **2024**, 35.

[74] F. Yang, P. Li, Z. Guo, X. Li, J. Zhao, L. Wang, Z. Zhong, *International Journal of Solids and Structures* **2024**, 305.

[75] J. Wu, F. Yang, C. Bai, J. Min, Z. Song, H. Fan, *Virtual and Physical Prototyping* **2025**, 20.

[76] Z. Hu, Z. Wei, K. Wang, Y. Chen, R. Zhu, G. Huang, G. Hu, *Nature Communications* **2023**, 14.